



# Faster Intercalation Pseudocapacitance Enabled by Adjustable Amorphous Titania Where Tunable Isomorphic Architectures Reveal Accelerated Lithium Diffusivity

Wessel van den Bergh,<sup>[a]</sup> Taylor Larison,<sup>[a]</sup> Maximiliano Jesus Jara Fornerod,<sup>[b]</sup> Stefan Guldin,<sup>[b]</sup> and Morgan Stefk<sup>\*[a]</sup>

Intercalation pseudocapacitance is a faradaic electrochemical phenomenon with high power and energy densities, combining the attractive features of capacitors and batteries, respectively. Intercalation pseudocapacitive responses exhibit surface-limited kinetics by definition, without restriction from the collective of diffusion-based processes. The surface-limited threshold (SLT) corresponds to the maximum voltage sweep rate ( $v_{SLT}$ ) exhibiting a predominantly surface-limited current response prior to the onset of diffusion-limitations. Prior studies showed increased lithium diffusivity for amorphous titania compared to anatase. Going beyond prior binary comparisons, here a continuum of amorphous titania configurations were prepared using a series of calcination temperatures to tailor both

amorphous character and content. The corresponding amorphous-phase  $v_{SLT}$  increased monotonically by 317% with lowered calcination temperatures. Subsequent isomorphic comparisons varying a single transport parameter at a time identified solid-state lithium diffusion as the dominant diffusive constraint. Thus, performance improvements were linked to increasing the lithium diffusivity of the amorphous phase with decreased calcination temperature. This remarkably enabled 95% capacity retention ( $483 \pm 17$  C/g) with 30 s of delithiation (120 C equivalent). These results highlight how isomorphic sample series can reveal previously unidentified trends by reducing ambiguity and reiterate the potential of amorphization to realize increased performance in known materials.

## Introduction

Electrochemical energy storage is growing quickly with increased demand for new materials with higher energy densities and higher power densities for faster (dis)charging capabilities.<sup>[1–3]</sup> This demand is particularly high for mobile devices and electric vehicles where faster charging is desired. These concomitant requirements reveal a gap between typical batteries and capacitors which offer, respectively, only high energy density or only high power density.<sup>[4–6]</sup> Here intercalation is defined as the insertion of a species within a host material. The term intercalation pseudocapacitance<sup>[7]</sup> describes the same process but specifically with electrochemical kinetics corresponding to surface limitations. Intercalation pseudocapacitive responses exhibit surface-limited kinetics by definition,

where the current response is proportional to the voltage sweep rate ( $v$ ).<sup>[8,9]</sup> Materials that have exhibited intercalation pseudocapacitive responses have sufficiently fast solid-state diffusion and an absence of phase transitions upon intercalation.<sup>[7–14]</sup> The introduction of dopants or other defects have been used to increase the rates of solid-state diffusion with examples for  $\text{Cu}[\text{Fe}(\text{CN})_6]_{0.63}\square_{0.37}\cdot 3.4\text{H}_2\text{O}$ ,<sup>[15]</sup>  $\text{T-Nb}_2\text{O}_5$ ,<sup>[16–18]</sup>  $\text{MoO}_3$ ,<sup>[19]</sup>  $\text{TiO}_2$ ,<sup>[20,21]</sup> and others.<sup>[22,23]</sup> Nanoscale materials can also differ from bulk analogs, for example, nanoscale anatase can lithiate as a solid solution whereas larger anatase crystals undergo a phase separation of discrete lithium rich and lithium poor domains.<sup>[24,25]</sup> The observation of intercalation pseudocapacitance depends upon both the intrinsic material properties (insertion rate, diffusivity, etc.) and on extrinsic architectural properties (surface area, transport constraints for electrons, electrolyte ions, and intercalation).<sup>[26–30]</sup> Generally pseudocapacitive current responses are observed from low  $v$  up until  $v$  is sufficiently high to onset diffusive-constraints, termed the surface-limited threshold (SLT,  $v_{SLT}$ ,  $t_{SLT}$ ). It often remains a challenge, however, to identify which specific diffusive process(es) limits the  $v_{SLT}$ . It follows that many works on nanoscale pseudocapacitive devices emphasize performance without identifying limitations from a specific diffusive process. From a perspective of electrochemical characterization, most diffusive processes (electron transport, electrolyte ion transport, and lithium intercalation) follow Fick's second law and thus all have similar  $(Dt)^{0.5}$  dependence which adds ambiguity to cyclic voltammetry (CV),<sup>[31]</sup> electrochemical impedance spectroscopy (EIS),<sup>[32–37]</sup> and 3D bode plot interpretations.<sup>[28,38]</sup> Though computational models<sup>[39–41]</sup> can in principle explain each aspect

[a] W. van den Bergh, T. Larison, Prof. M. Stefk  
Department of Chemistry and Biochemistry  
University of South Carolina  
Columbia, SC 29205, USA  
E-mail: morgan@stefikgroup.com

[b] M. Jesus Jara Fornerod, Prof. S. Guldin  
Department of Chemical Engineering  
University College London  
Torrington Place, London WC1E 7JE,  
UK

 Supporting information for this article is available on the WWW under  
<https://doi.org/10.1002/batt.202200122>

 © 2022 The Authors. *Batteries & Supercaps* published by Wiley-VCH GmbH. This is an open access article under the terms of the Creative Commons Attribution Non-Commercial License, which permits use, distribution and reproduction in any medium, provided the original work is properly cited and is not used for commercial purposes.

of device performance, they unfortunately require numerous parameters to be known, limiting their utility for studying unknown materials. From an architectural perspective, the ambiguity from concomitant diffusive processes sharing the same  $(Dt)^{0.5}$  dependence may be resolved by comparing samples where a single transport process is altered at a time, e.g. by comparing series of isomorphic samples.<sup>[27]</sup> In contrast, most methods used for preparing nanomaterials for electrochemical devices result in multiple architectural parameters changing at the same time, e.g. simultaneous changes to both the intercalation length and the pore size. For example, a series of T–Nb<sub>2</sub>O<sub>5</sub> nanoscale architectures were recently examined one variable at a time to identify that  $v_{SLT}$  was principally limited by solid-state lithium diffusion and varied with the intercalation length.<sup>[27]</sup> This extrinsic dependence is important to understand performance limitations as well as to support the optimization of energy devices.

Amorphization has emerged as an approach to modify, and sometimes increase, the rate of solid-state diffusion within known materials. Here amorphization is broadly defined and spans the continuum from disorder to perfect crystals. For example, the deliberate introduction of oxygen vacancies and dopants to intercalation materials have increased Li diffusivity,<sup>[16,17,23]</sup> electronic conductivity,<sup>[42,43]</sup> or both.<sup>[18–20]</sup> Dopants can provide shallow electron donors for enhanced electronic conductivity.<sup>[18,42,44]</sup> Improved electronic conductivity can improve ionic conductivity when lithium diffusion is coupled with electron transport in cases where  $D_{Li} > D_{e-}$ .<sup>[45]</sup> Vacancies similarly provide shallow electron donors which can increase electronic conductivity<sup>[16,19,20,43]</sup> and increase free-volume,<sup>[19]</sup> both of which can enhance Li diffusivity. Oxygen vacancies were reported to increase the interlayer spacing and the corresponding lithium diffusivity of MoO<sub>3-x</sub>,<sup>[19]</sup> and simulations of oxygen vacancies in V<sub>2</sub>O<sub>5</sub> found a lower energetic hopping barrier thus greater lithium diffusivity.<sup>[46]</sup> Similar comparisons were made between amorphous and crystalline TiO<sub>2</sub> which identified amorphization as route to lower the activation energy for solid-state diffusion.<sup>[29,47,48]</sup> It is worth emphasizing that there exists a continuum between an amorphous solid and a perfect crystal. While binary comparisons of “crystalline” vs “amorphous” material have provided inspiration, there remain few insights from more granular investigations. For example, of the infinite versions of “amorphous” material it is not clear yet if they exhibit markedly different electrochemical behaviors. For materials, such as nanoscale TiO<sub>2</sub> architectures which have been observed to stubbornly consist of a mixture of amorphous and crystalline components,<sup>[49–53]</sup> it is challenging to isolate the contribution and character of each phase.<sup>[8,54,55]</sup> Here a sol-gel process was used to prepare amorphous titania from precursors where the extent of amorphization was monotonically reduced with a progressive series of calcination heat treatments. The well-known and distinct voltammetric profiles for amorphous and anatase TiO<sub>2</sub> enable changes within the amorphous phase to be independently tracked. Comparing the performance of a tailored series of isomorphic architectures is ideal to limit

ambiguity by identifying specific diffusion-limited contributions when examining the effects of amorphization.

Persistent micelle templates (PMTs) enable the synthesis of tunable isomorphic architectures with nanoscale pores.<sup>[27,56–62]</sup> In brief, PMTs are kinetically trapped block polymer micelles that are used as templates to yield sample series with constant pore size. Varying the ratio of material precursors to micelle templates (material:template ratio, M:T) directly controls the final wall thickness while preserving constant templated pore size. Such independent control is in contrasts with other block polymer-based approaches where equilibration often couples such material additions to changing pore sizes and often also changing morphologies.<sup>[63,64]</sup> Furthermore since PMTs preserve spherical templates, the resulting porous materials have a constant morphology (isomorphic) due to the simple sphere packing arrangement which maintains relatively constant tortuosity.<sup>[65–72]</sup> Here tortuosity is defined as the arc-chord ratio, i.e., the pathlength travelled within a sample divided by the direct end-to-end distance. The tortuosity value is generally constant for a given morphology and varies with morphology comparisons.<sup>[65–72]</sup> Here, PMTs are used to derive isomorphic TiO<sub>2</sub> architectures absent of electrochemical additives prone to side reactions which may confound architectural and material contributions.<sup>[73,74]</sup> These architectures are calcined at different temperatures to identify granular changes in the lithium diffusivity and pseudocapacitive kinetics of amorphous titania.

## Results and Discussion

First the physical characterization for the series of isomorphic architectures is described before examining their electrochemistry. The inclusion of series of isomorphic architectures that vary a single spatial parameter at a time is important later to support the deconvolution of concomitant processes and thus reduce the ambiguity of interpretations. Here PMTs were used to prepare the desired series of architectures based upon poly(ethylene oxide-*b*-butyl acrylate) (PEO-*b*-PBA) micelle templates dispersed in methanol (Supporting Information Figure S1, Table S1). In brief, the inclusion of a controlled water content was used prevent polymer chain exchange and thus impose a constant template diameter.<sup>[27,56–60]</sup> Material precursors (titania nanoparticles) were prepared ex-situ to preserve the necessary water content for kinetic micelle control.<sup>[56]</sup> These material precursors were added in various quantities to PMT solutions (material:template ratio, M:T) to independently control the material wall thickness while preserving constant average pore size. The prepared sample conditions spanned a 2-parameter matrix with M:T = 1.6, 2.1, or 2.6 and with calcination temperatures of 280 °C, 380 °C, or 600 °C. It is noted that previous works reported residual carbon can remain after calcination of inorganic-organic mixtures to yet higher temperatures.<sup>[75,76]</sup> Scanning electron microscope (SEM) images of the resulting samples are shown in Figure 1. Please note that a uniform color scheme is used throughout this manuscript with each M:T ratio having a distinct shade and each calcination temperature having a distinct hue. The SEM images

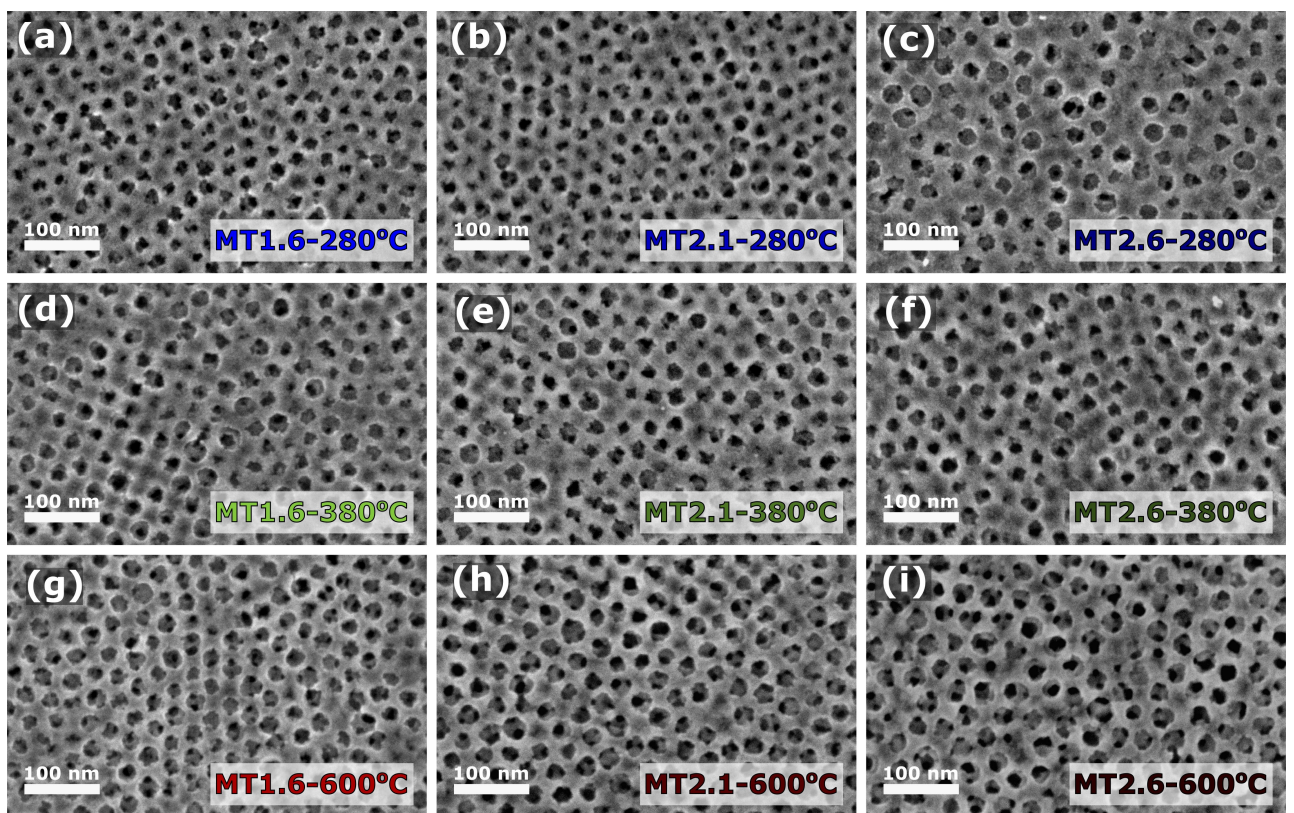


**Figure 1.** SEM images of the isomorphic series of mesoporous titania samples prepared with persistent micelle templates using different material:template (M:T) ratios and calcined at different temperatures. The M:T ratios and calcination temperatures are labelled on each panel. Subsequent figures preserve this color scheme with the hue corresponding to the calcination temperature and the shade corresponding to the M:T ratio.

showed randomly packed spherical, open pores (dark regions) with short-range order and material walls (light regions) that vary with M:T ratio. In these images, additional lower layers of pores and walls can be observed within most of the top surface pores for all samples. Small-angle X-ray scattering (SAXS) data from these samples are shown in Figure 2(a–c). These SAXS patterns exhibited a ~1:2 peak  $q$ -ratio which is consistent with the random sphere packing observed in SEM.<sup>[77]</sup> The SAXS patterns exhibited a similar number of structure factor peaks for all calcination temperatures indicating preservation of the nanostructure order (Figure S2). Furthermore, the SAXS peaks shifted to lower  $q$ -values ( $\text{nm}^{-1}$ ) with increasing M:T ratio. The corresponding trend in  $d$ -spacing values ( $d=2\pi/q$ ) thus indicates lattice expansion with increasing M:T ratio which is typical under PMT conditions and was well fitted by the PMT model (Equation S1, Figure 2d). The good fits of the PMT model further support the assertion of constant pore size which each series whose corresponding best-fit parameters are shown in Table S4. Numerous measurements were taken from SEM images to quantify the distribution of pore and wall dimensions. The average pore diameter was constant for each M:T series at constant calcination temperature. The average pore size increased somewhat with increasing calcination temperature (16.1% rel. change), likely corresponding to further densification of the wall material (Figure 2e). The porosity of these samples had little effect on electrolyte transport, vide

infra. The increasing average wall thickness with M:T measured by SEM was also well-matched by the best-fit of the PMT model (Figure 2f, Equation S3). For each given M:T value, the wall thickness decreased somewhat with increasing calcination temperature and was attributed to densification of the  $\text{TiO}_2$  during crystallization. The amorphous/crystalline character was evaluated using X-ray and electron scattering. Grazing-incidence wide-angle X-ray scattering (GI-WAXS) of M:T = 1.6 samples with many calcination conditions are shown in Figure 3(a). The scattering/diffraction pattern for the 280 °C calcination temperature had broad features (~22°–34°) that are consistent with the short-range atomic ordering of amorphous material. For calcination temperatures from 380 °C and higher there are peaks consistent with anatase crystallites (PDF 65-5714). The average anatase crystallite sizes are shown in Figure 3(b) based on Scherrer analysis of the (101) peak. The general trend was that increased M:T ratio and increased calcination temperature led to larger average crystallite sizes as expected, albeit with some deviations such as MT1.6–600 °C. The anatase crystallite dimensions were smaller than the wall thicknesses, for example, MT1.6–600 °C had 8.6 nm crystallites (Scherrer) within the  $15.15 \pm 0.23$  nm thick walls. This relationship was also apparent in brightfield and darkfield TEM, where MT1.6–600 °C exhibited an average of 6–7 nm crystallites (Figure S3a and b). Close examination of HR-TEM images also indicated random crystal placement throughout the nano-

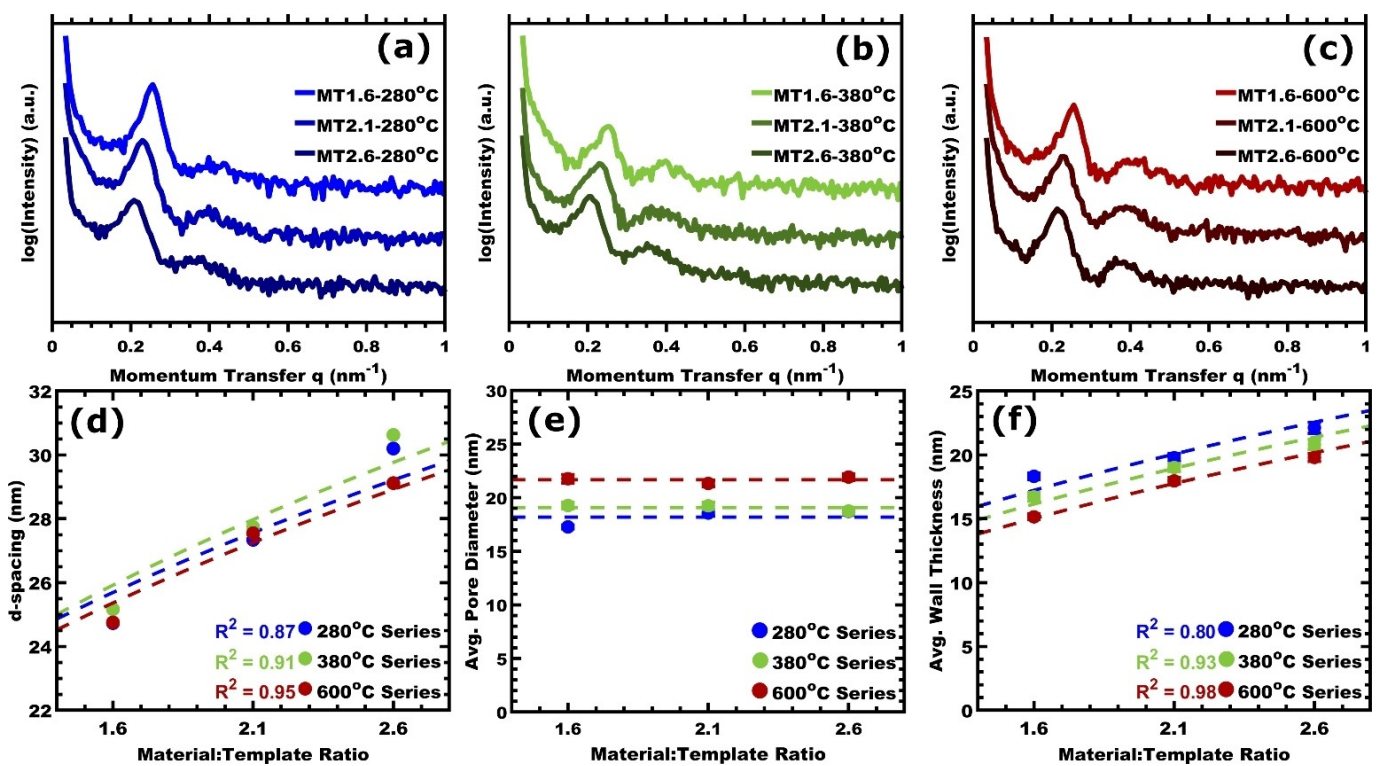
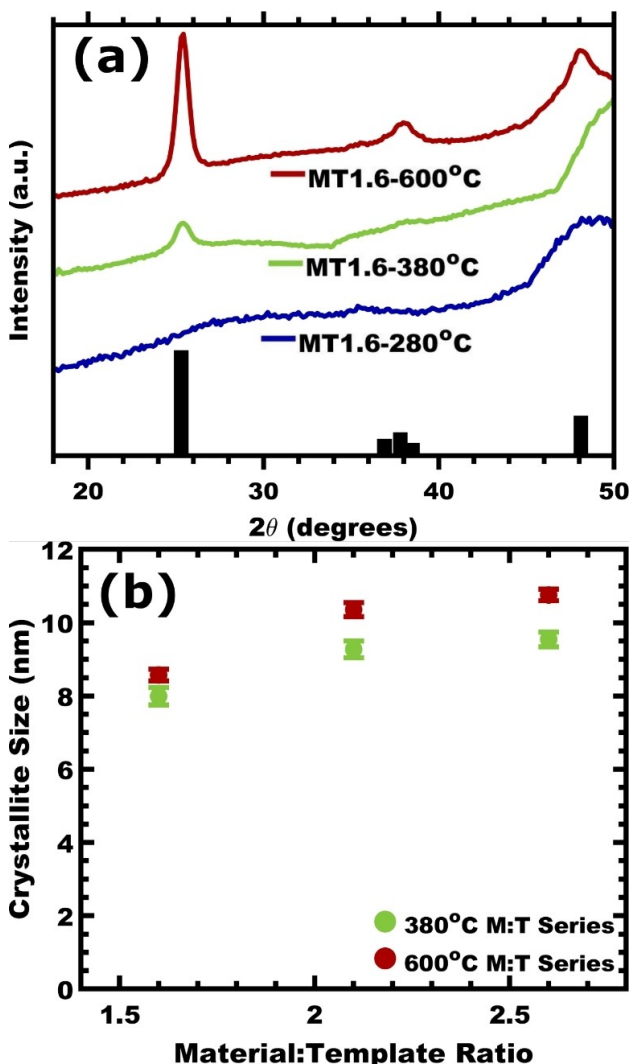


**Figure 2.** (a–c) SAXS patterns for all samples from the isomorphic series arranged by calcination temperature: a) 280 °C, b) 380 °C, and c) 600 °C. SAXS data were vertically offset for clarity. d) The corresponding d-spacing ( $2\pi/q^*$ ) trends reveal lattice expansion upon increasing material-to-template ratio (M:T). e) The mean pore diameters and f) mean wall thicknesses were determined from numerous measurements upon SEM images. The error bars correspond to the error-of-the-mean. D–f) Each of these metrics were compared to the PMT model (dashed lines) with goodness-of-fit ( $R^2$ ) indicated.

structure with an abundance of grain boundaries (Figure S3c). With a large fraction of amorphous phase in all samples determined electrochemically, vide infra, it is likely that the amorphous phase is also distributed throughout the nanostructure. Thus, the crystal growth observed with increasing calcination temperature was attributed to the progressive conversion of an initially amorphous phase to anatase. As the calcination temperature increases, changes are possible within the remaining amorphous phase since there is a continuum between disorder and perfect crystals that notably includes a continuum of amorphous configurations. Quantitative XPS analysis of O/Ti ratios from lattice O 1s and Ti 2p regions showed a monotonic decrease in  $x$  ( $\text{TiO}_x$ ) from 2.88 to 2.54 with increasing calcination temperature (Figure S5). This XPS trend indicates the progressive removal of O which is similar to that seen with sol-gel derived niobia.<sup>[78]</sup> Here we term the samples with the lowest calcination temperatures as thus having the greatest degree of amorphization for both the amorphous and anatase phases. Thus, a set of tailored isomorphic architectures were prepared with controlled pore size, titania wall thickness, and extent of amorphization.

Cyclic voltammetry (CV) was used to characterize lithiation behavior across the series of samples. All samples were measured with logarithmically spaced voltage sweep rates ( $v$ ) within the same 1.5–2.5 V vs. Li/Li<sup>+</sup> window using  $\text{LiClO}_4/\text{PC}$  electrolyte with a hold step for equilibration before reversing the voltage sweep direction. The CV data for the MT = 1.6 series

at 2.0 mV/s is shown first to describe changes with calcination temperature (Figure 4). Condition MT1.6–280 °C exhibited a broad peak at  $1.641 \pm 0.007$  V. Several prior reports of sol-gel derived  $\text{TiO}_2$  lithiation have included a similar CV feature that was sometimes ascribed to amorphous titania and was sometimes ascribed to  $\text{TiO}_2(\text{B})$ , a polymorph known to exhibit intercalation pseudocapacitance. Some of those reports described the  $\text{TiO}_2(\text{B})$  as being “X-ray amorphous,” i.e., without supporting diffraction data due to nanoscale crystals.<sup>[50–52, 56, 79–84]</sup> Since many definitions of “crystallinity” require observable diffraction,<sup>[85]</sup> it is suggested that such phases be termed “amorphous.” For the present samples, neither X-ray diffraction data nor additional electron diffraction measurements (SI Figure S4) were consistent with  $\text{TiO}_2(\text{B})$  so the CV feature near 1.6 V is ascribed to amorphous titania. The CV of MT1.6–380 °C included similar amorphous character with an additional anodic feature at  $2.061 \pm 0.011$  V and a complimentary cathodic peak at  $1.682 \pm 0.002$  V (379 mV peak separation), consistent with typical anatase lithiation.<sup>[24, 86]</sup> Yet higher calcination temperature led MT1.6–600 °C to have more prominent anatase peaks with less amorphous content (Figure 4). It is noteworthy that the amorphous peak shape seen in CV changes considerably with calcination temperature, having very broad character for MT1.6–280 °C and a narrow peak for MT1.6–600 °C, suggesting increased localization upon further calcination.<sup>[9, 10]</sup> The total lithiation capacity for these two samples were similar at 476.8 ± 17.34 C/g <sub>$\text{TiO}_2$</sub>  and 516.2 ± 15.53 C/g <sub>$\text{TiO}_2$</sub>  at 280 °C and 600 °C



respectively ( $v=2.5$  mV/s, Figure S6a, Table S1). Compared to the 604 C/ theoretical capacity for  $\text{Li}_{0.5}\text{TiO}_2$ , these capacities correspond to  $\text{Li}_{0.40-0.43}\text{TiO}_2$ . The fraction of lithiation current/capacity attributed to amorphous and anatase phases were determined by integration of the anatase peak upon the tail of the amorphous peak with a suitable baseline (Figure S7). Since all samples had similar gravimetric capacity regardless of amorphous content, the mass of the amorphous phase ( $g_{\text{amor}}$ ) was calculated as the product of the amorphous Coulombic fraction (Coul.%amor) with the titania mass ( $g_{\text{TiO}_2}$ ) determined via electrochemical integration (Figures S7, S8a and d). This amorphous coulombic fraction was consistent with the corresponding changes to the anatase WAXS (101) peak intensity (Figure S8c and f). Repeated CV cycles at 25.0 mV/s on all samples reported here revealed relatively constant lithiation capacity without apparent degradation (Figure S9). While both amorphous and anatase contributions were recorded, this

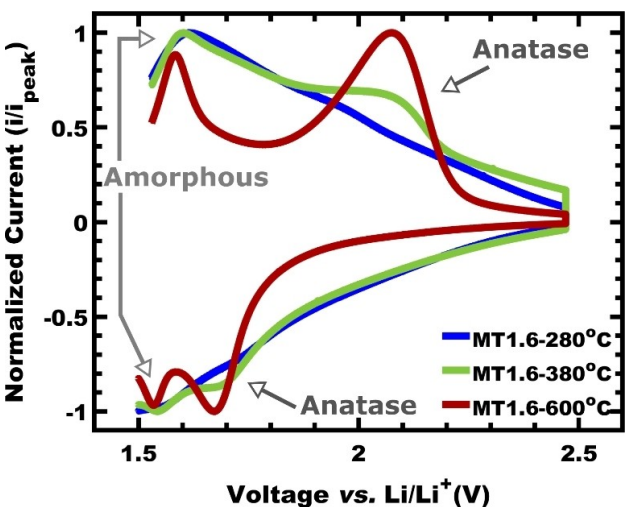


Figure 4. Normalized cyclic voltammograms of representative samples (M:T = 1.6) calcined at 280 °C, 380 °C, and 600 °C. The voltage window was 1. –2.5 V vs. Li/Li<sup>+</sup> with an electrolyte of 1 M LiClO<sub>4</sub> in propylene carbonate (PC) and a voltage sweep rate of 2 mV/s. The corresponding peaks from amorphous TiO<sub>2</sub> and anatase TiO<sub>2</sub> are indicated with arrows.

manuscript focuses on the changes to the character and performance of the amorphous phase.

The electrochemical kinetics were analyzed by comparing peak current densities to the voltage sweep rates. Series of CV data were acquired over a range of  $v$  (Figure 5a), and the corresponding amorphous phase peak currents were plotted on log-log axes (Figure 5b). First representative data from MT1.6-280 °C are described before making comparisons between sample conditions. CV current responses are often modeled with a power law relationship:<sup>[31]</sup>

$$i_p = av^b \quad (1)$$

where  $i_p$  is the peak current,  $a$  is a coefficient, and  $b$  ("b-value") is a power dependence. The b-value is useful to ascribe the type of rate-limiting process(es) where  $i \propto v$  ( $b=1.0$ ) indicates a dominant surface-limited process,  $i \propto v^{0.5}$  ( $b=0.5$ ) indicates a dominant semi-infinite diffusion-limited process, and intermediate values can indicate a convolution thereof. The noted log-log axes are convenient since the corresponding derivative yields the b-value as a function of  $v$  (b-value( $v$ )) and can thus indicate transitions of the type of rate-limiting process (Figure 5c). For example, the b-value for the amorphous phase is proximal to 1.0 for sweep rates up to ~40 mV/s, indicating surface-limited behavior. The combination of surface-limited kinetics with energy storage via intercalation warrant the behavior classification as intercalation pseudocapacitance. As  $v$  increases further, the b-value lowers from 0.9 to 0.7, indicating a progressively increasing contribution from a diffusion-limited process. Amorphous condition MT1.6-280 °C departs from surface-limited kinetics ( $b=0.9$ ) at  $v_{SLT}=42.86 \pm 0.04$  mV/s where  $b=0.9$ .<sup>[27]</sup> The  $v_{SLT}$  thus corresponds to the onset of diffusive limitations to the overall kinetics. Isomorphic series will later be compared to assign these diffusive limitations with specificity.

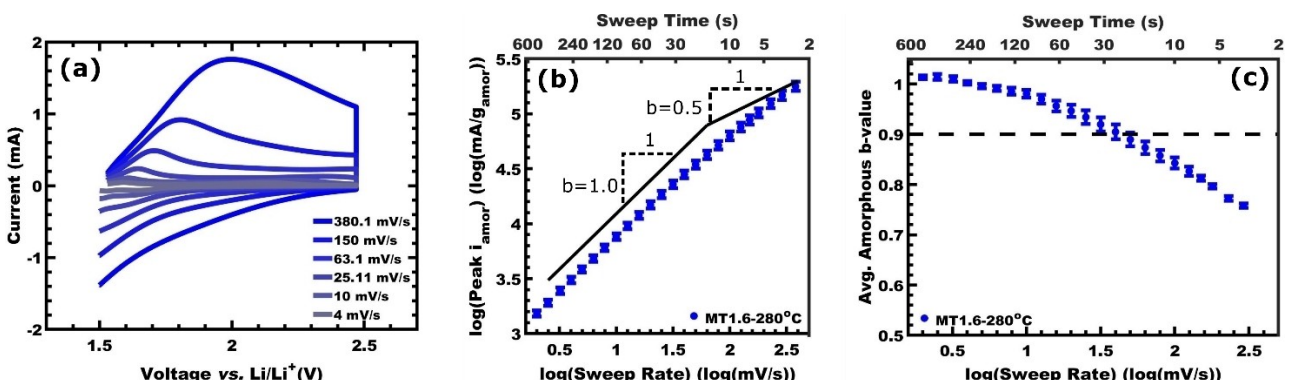


**Figure 5.** a) Representative cyclic voltammograms at different voltage sweep rates for sample MT1.6-280 °C. b) A log-log plot of the anodic amorphous peak current vs. voltage sweep rate. The amorphous current was normalized per g of total TiO<sub>2</sub> and per the coulombic % amorphous (Tables S5 and S6). The slope (*b*-value) of this log-log plot identifies the type of rate-limiting process. c) The corresponding derivative plots the *b*-value as a function of voltage sweep rate. The surface-limited threshold (SLT) denotes the departure from surface-limited kinetics (dashed line, *b*=0.9). Plotted points correspond to mean values  $\pm$  the standard error-of-the-mean.

Next attention is turned to changes within a given architecture as function of the extent of amorphization.

Samples with constant M:T ratio have nearly identical architecture and thus comparisons of the effects of different calcination temperatures largely reveal changes to the material itself. The amorphous peak current values and *b*-values(*v*) with calcination temperature alone are shown in Figure 6. Comparing peak currents with amorphous mass normalization at the lowest *v* (*b*≈1.0, 2.5 mV/s) provides an indication of the rate of the surface-limited step (Figure 6a, Figure S9). The temperature series MT1.6-280 °C-12hr and MT1.6-290 °C-12hr conditions, both purely amorphous by WAXS and CV, had no significant difference in peak current (*v*=2.5 mV/s) indicating a similar surface reaction rate (Figure 6a). In contrast, the *v*<sub>SLT</sub> for MT1.6-280 °C-12hr was 57.6% higher than that for MT1.6-290 °C-12hr (Figure 6b and c, Table S5), indicating a significant acceleration in the diffusion-limited process. Considering the nearly identical nanostructures, this change is most likely associated with the solid-state lithium diffusivity, an assessment that is later supported with additional experiments. With further increasing calcination temperature, the amorphous CV shape narrows (Figure 4), limiting peak current comparisons between the lowest and highest calcination temperatures. Comparison of amorphous mass normalized peak currents for MT1.6-420 °C-12hr, MT1.6-450 °C-12hr, and MT1.6-600 °C-1hr revealed no statistically significant difference, in contrast, MT1.6-420 °C-12hr had a 21.5% higher amorphous *v*<sub>SLT</sub> than MT1.6-600 °C-1hr, again indicating that the diffusion-limited process was fastest with the lowest calcination temperatures (Figure 6b and c, Table S5). Prior computational and experimental studies identified that amorphous titania can have faster solid-state lithium diffusion than anatase (binary comparison).<sup>[29,47,48]</sup> The present data indicate a further granular trend where the solid-state lithium diffusivity within the amorphous phase decreases monotonically with calcination temperature. The identity of this specific diffusion-limited process is examined next amongst several candidates.

A series of CV experiments controlling electrolyte concentration, film thickness, and wall thickness were performed to identify the effects of each diffusive transport process upon the electrochemical kinetics of amorphous titania. The lithium-ion transport rate from the electrolyte depends upon the path-length, the volume fraction of pores, and the Li ion concentration. Architectures with the lowest volume fraction of pores (M:T=2.6) were examined as the most challenging case for electrolyte transport. The same CV and *b*-value analysis were performed for conditions MT2.6-280 °C, MT2.6-380 °C, and MT2.6-600 °C in both 1.0 and 0.5 M LiClO<sub>4</sub> (Figures S10d-f, S11a-d, and Table S6). The change in electrolyte concentration did not lead to any significant changes in amorphous peak current nor in *v*<sub>SLT</sub>, indicating that these electrolyte concentrations neither alter the surface-limited reaction rate nor the diffusive electrolyte lithium-ion transport. Next electron transport was examined by altering the film thickness. A 28% increase in film thickness (Figure S12, Table S7) did not significantly affect the amorphous mass normalized peak current and lead to a general, minor (few mV/s) decreases in the amorphous *v*<sub>SLT</sub> for MT2.6-280 °C, MT2.6-380 °C (Figure S11a). For completeness' sake it is noted that the film thickness affects both electrolyte transport and electron transport, however the lack of electrolyte constraints with a larger 50% change in concentration suggests that the observed minor diffusive constraint from film thickness is associated with electron transport alone. Lastly, wall thickness was independently adjusted to vary the solid-state diffusion pathlength by comparing three different M:T ratios at each calcination temperature. Starting with the 280 °C M:T series, there was no significant change in amorphous peak current which was surprising that the surface-limited process did not slow down with the reduction of specific surface area that geometrically accompanies thickening of walls (Figure 7a). This reduction in specific porosity with increasing M:T is also apparent in the changing refractive index values (Table S7). Here the similar surface-limited kinetics could be associated with microporosity within the walls and pore roughness (Figure S13) due to the

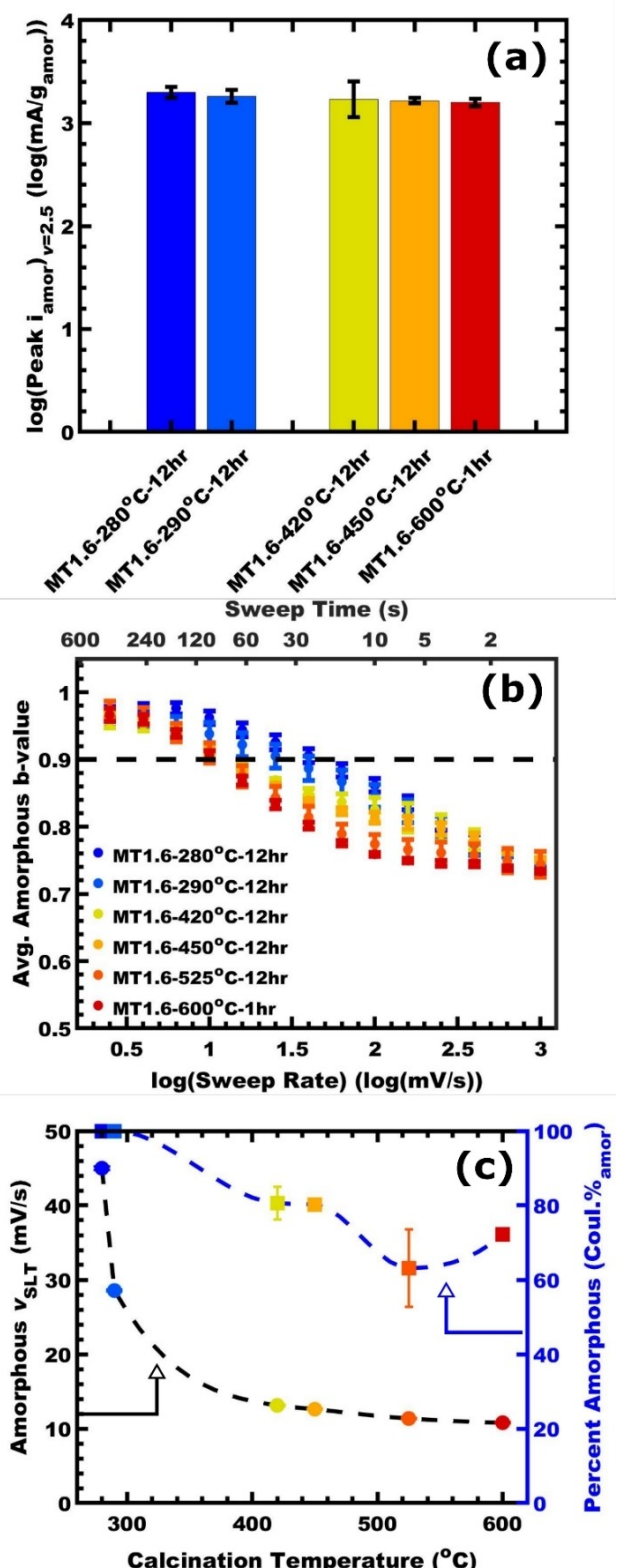


**Figure 6.** Comparisons of M:T = 1.6 samples calcined at different temperatures: a) amorphous peak currents at  $v = 2.5$  mV/s, b) amorphous b-value( $v$ ), c)  $v_{\text{SLT}}$  and coulombic amorphous content. All plotted points correspond to mean values  $\pm$  the standard error-of-the-mean.

limited thermal coarsening, thus the surface area may increase with M:T. For this series, the amorphous  $v_{\text{SLT}}$  increased

significantly from  $23.48 \pm 0.073$  to  $42.86 \pm 0.04$  mV/s with decreasing M:T, corresponding to thinning the wall and decreasing the intercalation length (Figure 7b, Table S6, Figure S10a). The maximum  $v$  preserving 95% of the total capacity ( $v_{95\%}$ ) similarly increased from  $96.89 \pm 0.48$  to  $203.4 \pm 2.82$  mV/s with thinner walls (Figure 7e). Both of these large kinetic changes with wall thickness confirm that solid-state lithium diffusion is the dominant diffusive limiting process. The M:T series calcined at 380 °C and 600 °C both exhibited a decrease in amorphous mass normalized peak current, indicating the expected decrease in the surface-limited rate when the specific surface area is reduced (Figure 7a, c and d, Table S6, Figure S10b and c). The 380 °C series exhibited a similarly large increases in amorphous  $v_{\text{SLT}}$  and increase in total  $v_{95\%}$  with decreasing wall thickness, again indicating that solid-state lithium diffusion is the dominant diffusive constraint. The 600 °C series, however, exhibited minor variation of amorphous  $v_{\text{SLT}}$  and an increase in total  $v_{95\%}$  with decreasing wall thickness. The lack of a simple  $v_{\text{SLT}}$  trend for the 600 °C series may be associated with changes to the spatial distribution of the amorphous phase at this high calcination temperature. Please note that the amorphous  $v_{\text{SLT}}$  trend for the 600 °C series was consistent across multiple samples, multiple batches, and repeated measurements and is similar to the value for the closely related sample MT1.6-600 °C-1hr (Figure 6c). The trend in total  $v_{95\%}$  for the 600 °C series is likely associated with the significant anatase content (13.4% increase of the total capacity). These changes in  $v_{\text{SLT}}$  and  $v_{95\%}$  are next compared to quantitative expectations.

The generalized relationship of spatial dimensions to the rates of diffusion-limited process may be estimated using Fick's second law for 1D diffusion with an infinite source<sup>[27]</sup>:

$$x \propto (Dt)^{0.5} \quad (2)$$

where  $x$  is the diffusion length (half the concentration of the source),  $D$  is diffusivity, and  $t$  is time. With CV the sweep time ( $t$ ) may be calculated as the voltage window divided by  $v$ . Likewise the maximum diffusion length corresponds to half of the wall thickness. Plots of  $t^{0.5}$  vs. the intercalation length (half wall thickness) are thus expected to yield a linear trend. The amorphous  $v_{\text{SLT}}$  follows these expectations (EQ2) for both the 280 °C and 380 °C sample series both with  $R^2$  values of 0.99. As noted earlier the 600 °C series did not exhibit monotonic variation of amorphous  $v_{\text{SLT}}$  (Figure 8a). Comparison of samples MT1.6-600 °C to MT2.6-380 °C with similar amorphous content and thicker walls emphasizes the significant increase in solid-state lithium diffusivity for lower temperature calcinations where there is an 86.1% increase in the amorphous  $v_{\text{SLT}}$  (Figure 8f). The trends for  $t_{95\%}$  cleanly corresponded to the linear expectations of EQ2 with  $R^2 > 0.94$ , again supporting solid state lithium diffusion as the dominant diffusive constraint (Figure 8b). Please note that the amorphous  $t_{\text{SLT}}$  values correspond to the behavior of the amorphous phase alone since the peak currents were not convolved with anatase contributions until higher  $v$ -values exceeding the amorphous  $v_{\text{SLT}}$  (Figure S14). Briefly, the trends in crystalline anatase

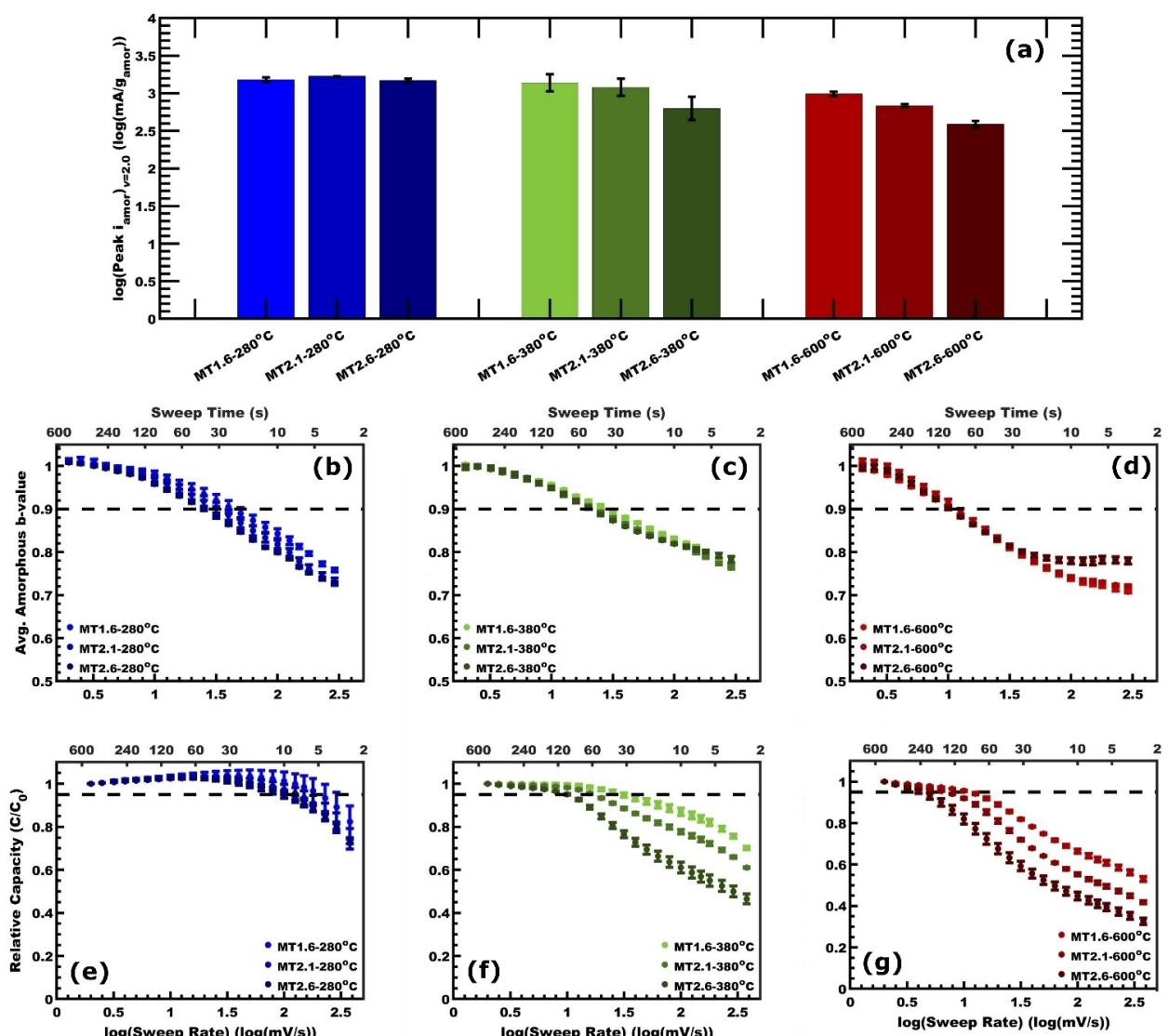


**Figure 7.** Amorphous titania kinetic constraints from the intercalation length (wall thickness) were examined over a range of isomorphic architectures (indicated M:T values) with different calcination conditions: b, e) 280 °C, c, f) 380 °C, and d, g) 600 °C. Comparisons include a) amorphous peak currents, b–d) amorphous b-values(v) and e–f) relative capacity values(v). Values are presented as the mean  $\pm$  standard error-of-the-mean.

behavior are examined. Both the 380 °C and 600 °C series exhibited similar crystalline anatase peak currents for all calcination temperatures within the error of the measures (Figures S16 and S17). In both cases, the b-value(v) decreases monotonically towards  $b=0.6$  with thicker walls, consistent with increasing rate limitation by solid-state diffusion. Comparing the anatase phase b-values(v) of 600 °C to those for 380 °C suggests faster solid-state lithium diffusion for crystalline anatase with more amorphization or alternatively accelerated kinetics from faster nearby amorphous regions.<sup>[87]</sup> Thus the collection of electrochemical kinetic data indicate that solid state lithium diffusion was the dominant diffusive constraint for these architectures.

Lastly, the material performance of MT1.6-280 °C-12 hr, consisting of only active material on a current collector, was compared to high-performing TiO<sub>2</sub> precedents reported in the literature, many of which contained conductive carbon and

binder additives.<sup>[29,88–91]</sup> All comparisons were done by normalizing by active material which gives some advantage to conditions which did include additives. This includes ALD-prepared macroporous (2 nm) amorphous TiO<sub>2</sub> on Au,<sup>[29]</sup> hydrothermal TiO<sub>2</sub>(B) nanowires (75:18:7, active:carbon:binder),<sup>[88]</sup> anatase/graphene (50:2 weight ratio, 80:10:10, active:carbon:binder),<sup>[89]</sup> electrospun anatase nanotubes (direct deposit on Cu),<sup>[90]</sup> and amorphous TiO<sub>2</sub>/graphene (150:1 weight ratio, 85:10:5, active:carbon:binder).<sup>[91]</sup> Figure 9 shows the C-rate dependent capacity of these materials. Here C-rate is defined with respect to the inverse of the (dis)charge time, e.g., a 1 hr (dis)charge is a 1 C rate whereas a 1-minute time (1/60<sup>th</sup> hr) (dis)charge corresponds to a 60 C rate. While C-rate capacities are often measured under galvanostatic conditions, CV data can be analogously presented in terms of C-rate based on the inverse of the sweep time. The general trend is a decrease in capacity with increasing C-rate where the literature precedents

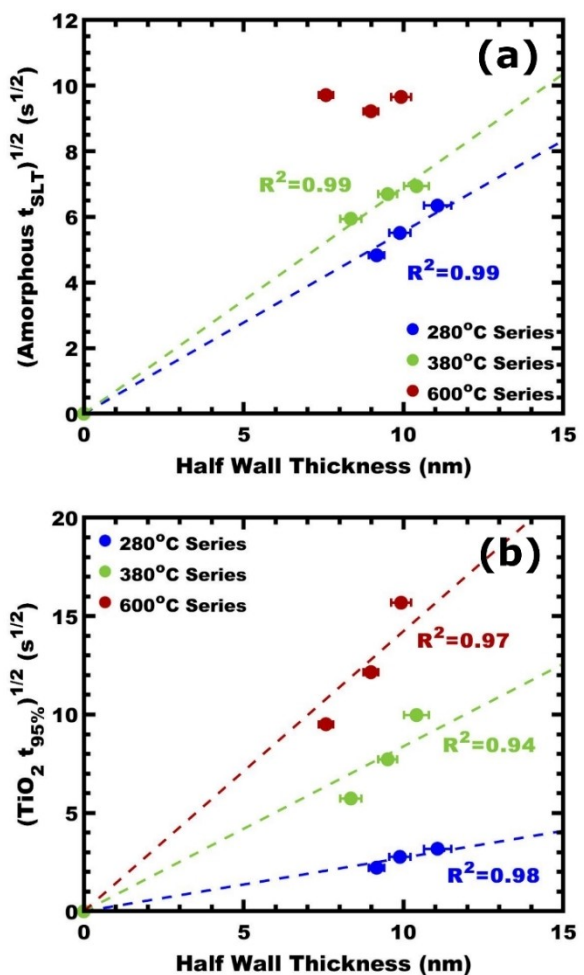


**Figure 8.** Amorphous titania electrochemical kinetic metrics were compared as a function of the intercalation length (M:T ratio) and calcination temperature. Both plots of a)  $t_{SLT}^{0.5}$  and b)  $t_{95\%}^{0.5}$  vs. half wall thickness (intercalation length) should yield linear plots for generalized diffusion-limited processes with  $\propto \sqrt{Dt}$ , see Equation (2). Values are presented as the mean  $\pm$  standard error-of-the-mean.

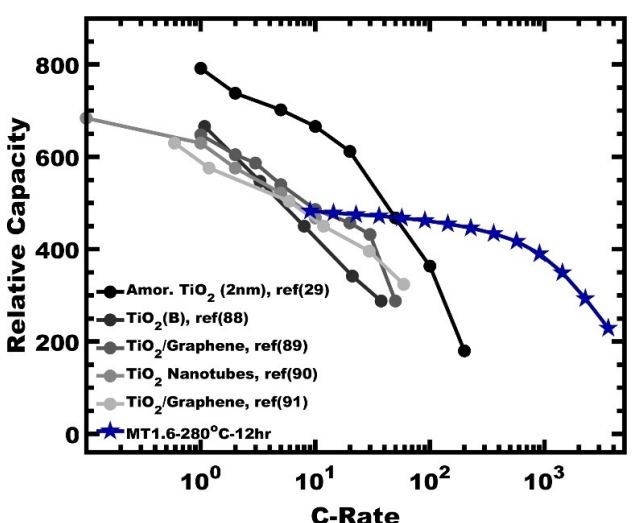


**Figure 9.** The rate-dependent lithiation capacity of MT1.6-280°C-12 hr is compared to published titania precedents as a function of C-rate.

here reached 400 C/g between 15–80 C-rate, generally due to diffusion constraints. In contrast, condition MT1.6-280°C-12hr with enhanced amorphous titania diffusivity maintained >400 C/g up to an 800 C-rate (4.5 s). This performance is remarkable considering that the sample was free from conductive additives and was ~50 vol% dense oxide yet demonstrated significant capacity retention with an order of magnitude faster charge rates. With the performance of amorphous materials depending significantly upon the underlying atomic structure (i.e., the extent of amorphization), there is a significant opportunity for future works to characterize the specific atomic structure aspects that lead to such improved electrochemical behaviors as well as synthetic opportunities to prepare pure amorphous (also pure crystalline) samples with deliberately tuned extents of amorphization. Furthermore, the integration of such high-performance materials with traditional slurry electrodes has opportunities for further innovation outside the scope of this manuscript.<sup>[92]</sup> The granular extents of amorphization examined here suggest a rich area for additional materials research advancing energy storage devices.

## Conclusion

Amorphization is a promising approach to accelerate lithium diffusivity in both amorphous and anatase TiO<sub>2</sub>. The increase of lithium diffusivity enables amorphous titania to exhibit intercalation pseudocapacitive responses with higher voltage sweep rates, enabling access to faster (dis)charge rates with comparable capacity. Going beyond prior binary comparisons, the present study reveals granular changes to both amorphous and anatase titania as a function of calcination conditions, reflecting the underlying extended continuum between perfect crystals and amorphous disorder. A 317% increase in amorphous  $v_{SLT}$  corresponding to an increase in lithium diffusivity, was found for samples calcined at 280 °C as compared to those at 600 °C. Notably, there were not apparent changes in the surface reaction rate for the amorphous phase as a function of the calcination temperature (fixed M:T, constant nominal specific surface area). The kinetic effects resulting from changes to each of the underlying diffusive transport processes revealed no sensitivity to electrolyte transport, a minor sensitivity to electron transport and a dominant diffusive constrain from intercalation through the wall thickness. Multiple kinetic metrics were compared to the distance-time (intercalation length  $\propto t^{0.5}$ ) relationship estimated from a simple solution to Fick's second law of diffusion. The temperature dependent behavior of the amorphous phase revealed that its character is sensitive to its degree of disorder, i.e., the degree of amorphization. The corresponding top performer MT1.6-280 °C exhibited 95 % capacity retention (483 ± 17 C/g) with sweep times less than 30 seconds, comparable to a remarkable C-rate of 120 C. This study shows how isomorphic sample series can reveal previously unidentified trends and reduce ambiguity amongst diffusion-limited processes that all share the same fundamental  $Dt^{0.5}$  dependence.

## Experimental

### Materials

Methanol (MeOH, 99.8%, Fisher) was dried at room temperature by storage over 30% w/v of molecular sieves (3 Å, 8–12 mesh, Acros Organics) for a week.<sup>[53]</sup> Copper(I) bromide (99.99%, Aldrich), tris-(2-dimethylaminoethyl) amine (97%, Aldrich), dry lithium perchlorate (LiClO<sub>4</sub>, 99.99%, Aldrich), anhydrous propylene carbonate (99.7%, Aldrich), titanium(IV) isopropoxide (TTIP, ≥98%, Acros Organics) were used as received and stored inside an argon-filled glove box. n-Butyl acrylate (+99%, Acros Organics) monomer was passed through basic alumina column just prior to use. 2-Bromopropionic acid (>99%, Aldrich), chloroform (>99.8%, VWR) stabilized with amyrene, 4-(dimethylamino) pyridine (+99.0%, TCI America), dimethylformamide (97%, Aldrich), poly(ethylene glycol) methyl ether (PEO-OH,  $M_n=5,000$  g/mol, Aldrich), hexane (>98.5%, Fisher), concentrated hydrochloric acid (HCl, 37% w/w, ACS grade, VWR), tetrahydrofuran (Fisher, Certified) were used as received.

### Polymer Synthesis

Poly(ethylene oxide)-*b*-poly(n-butyl acrylate), PEO-*b*-PBA, diblock polymer was synthesized by a two-step synthesis. A Steglich esterification of poly(ethylene glycol) methyl ether synthesized the macroinitiator, followed by an atom transfer radical polymerization to create the PHA block. The synthesis is described elsewhere in detail.<sup>[56]</sup> The molar mass of PBA was determined using a Bruker Avance III HD 300 <sup>1</sup>H NMR by comparing it to the PEO methyl ether starting material ( $M_n=5.0$  kg/mol) (Figure S1a). The molar mass dispersity was characterized using a Waters gel permeation chromatograph (GPC) equipped with a Waters 1525 binary pump, three styragel columns (HR1, HR3, HR5 in the effective molecular weight range of 0.1–5, 0.5–30, and 2–400 kg/mol, respectively), and a Waters 2414 refractive index detector with THF as the carrier solvent. The GPC was calibrated with poly(styrene) standards (1.50, 3.28, 10.00, 17.40, 32.70, 120.00, 214.00, 545.00, 1010.00 kg/mol) obtained from Polymer Standards Service GmbH. GPC samples were prepared in THF at concentrations of 5 mg mL<sup>-1</sup>, filtered through a 0.2 µm PTFE syringe filter prior to injection (Figure S1b).

### PMT synthesis

A micelle template stock solution was prepared by dispersing PEO-*b*-PBA (25 mg) in MeOH (2.5 mL) before adding concentrated HCl was added slowly to reach 0.7 wt% with respect to the total mixture (PEO-*b*-PBA, MeOH, and HCl). After acid addition, the solution was placed in sonication bath Fisher ultrasonic bath (Cat. no. FS-28) operated continuously at full power (225 W) and frequency of 40 kHz for 10 min at room temperature to enable chain exchange under kinetically limited condition.<sup>[60,94]</sup>

An ex-situ TiO<sub>2</sub> sol stock was used as described in detail elsewhere.<sup>[56]</sup> Briefly, 5 mL of titanium isopropoxide (TTIP) was added to 1.2 mL of rapidly stirring concentrated HCl (37 wt%), creating a solution with a 3:1 H<sub>2</sub>O/Ti ratio. Note that this reaction is very exothermic. After being allowed to cool for a few minutes, 2 mL of anhydrous MeOH was added to dilute the sol stock solution. This dilute sol stock solution was combined with the micelle template stock solutions described above in varying ratios, depending on the target material to template (M:T) ratio. Here, the M:T ratio is calculated by comparing the anticipated final oxide mass (TiO<sub>2</sub>) relative to the mass of the block polymer template. Each film was spin coated for 30 sec at 1,100, 1,100, and 2,00 rpm under 36% relative humidity for each M:T ratio of 1.6, 2.1, and 2.6, respectively as described elsewhere in detail.<sup>[58,60,95]</sup> Immediately

after spin coating, each sample was removed from the humidity-controlled chamber and placed on a 250 °C hot plate overnight, after which the samples were aged at 110 °C until they were prepared for calcination. This processes, termed as “aging,” is meant to crosslink the metal oxide were optimized to prevent dewetting and sufficient crosslinking to survive calcination. After each spin coating of a sample, the humidity-controlled spin coating chamber was replaced to avoid residual solvent vapor, as described previously.<sup>[58]</sup> Glass, silicon, and fluorine doped tin oxide (FTO) substrates were used for SAXS; SEM, Ellipsometry, and TEM; and electrochemistry and ICP-MS, respectively. All samples were calcined with a ramp rate of 5 °C/min to 200 °C followed by a ramp rate of 10 °C/min to the specified temperature denoted by sample name, which was held for 12 h, except for MT1.6-600 C-1hr which was held for 1 hr and allowed to cool to room temperature.

### Ellipsometry

Visible light ellipsometry measurements were done with a J.A. Woollam Co. V-VASE ellipsometer. Si substrates coated with TiO<sub>2</sub> architectures calcined at 450 °C for 0.1 hr at a ramp rate of 5 °C/min to 200 °C followed by a ramp rate of 10 °C/min, prepared at different spin coating RPM, were measured from 450 to 1000 nm (Δ2 nm) at incident angles of 64, 69, and 74 degrees intending to be below, near, and above Brewster’s angle for TiO<sub>2</sub> collecting both  $\Delta$  and  $\Psi$  data. Data analysis was done using Semilab’s Spectroscopic Ellipsometry Analyzer (v1.6.6) with the optical model consisting of a Si substrate and a single phase on top whose thickness was determined via Cauchy’s dispersion law.<sup>[96]</sup> The refractive indices used to determine porosity was estimated from literature for both nanoscale anatase,<sup>[97]</sup> amorphous,<sup>[98]</sup> and their effective mean contributions<sup>[99,100]</sup> at 632.8 nm.

### X-ray scattering experiments

X-ray experiments were conducted using the SAXSLab Ganesha at the South Carolina SAXS collaborative (SCSC). A Xenocs Genix 3D microfocus source was used with a copper target to produce monochromatic beam with a 0.154 nm wavelength. The instrument was calibrated prior to measurements using National Institute of Standards and Technology (NIST) reference material, 640d silicon powder with peak position at  $2\theta=28.44^\circ$ . A Pilatus 300k detector (Dectris) was used to collect the 2D scattering patterns with nominal pixel dimensions of 172×172 µm. SAXS data were acquired with an X-ray flux of ≈3.0 M photon per second upon the sample and a detector-to-sample distance 950 mm. Transmission SAXS data were measured to observe the purely in-plane morphology. The 2D images were azimuthally integrated to yield the scattering vector and intensity. GI-WAXS measurements were conducted with an incident angle ( $\alpha$ ) of 8° relative to the incident beam. The GI-WAXS sample-to-detector distance was X mm with an X-ray flux of ≈38.0 M photon per second upon the sample. A Gaussian point-spread function was utilized to interpret scattering data from grain-size broadening per the Scherrer formula.<sup>[101,102]</sup>

### XPS

XPS measurements were conducted using a PHI VersaProbe III with a monochromatic Al K $\alpha$  source (1486.7 eV). Measurements consisted of a survey of 3 sweeps collected with a pass energy of 280 eV. X-ray beam was set to 25 W, 15 kV with a 100 µm diameter which was rastered over a 500×500 µm square. Peak fitting was done with Gaussian-Lorentzian method with the FWHM constrained to 1.35–1.5 eV. Samples were calibrated to C at 284.8 eV.

## SEM

Top-view images of calcined films were acquired with a Zeiss Gemini500 field emission SEM using an accelerating voltage of 5 keV and an in-lens secondary electron detector. The working distance was maintained at  $\approx$ 4.5 mm and images were acquired at constant 1500 kX magnification. At least 100 measurements were made for each feature (pores and walls) for each condition (temperature and M:T ratio) to determine their statistical metrics using ImageJ software. The wall thickness was measured as the diameter on an inscribed circle between neighboring pores as described elsewhere,<sup>[56,62]</sup> in addition pore diameter was measured using an inscribed circle method. Pore size and wall thickness are presented as an average  $\pm$  standard-error-of-the-mean.

## TEM

TEM images were acquired using a JEOL 1400 Plus TEM operated in bright field, dark field, and diffraction mode with an accelerating voltage of 120 keV. Samples were prepared by placing a single drop of solution containing suspended mesoporous film, scraped from their substrates with glass, onto a carbon coated 300 mesh copper grids purchased from Electron Microscopy Sciences. The solution was allowed to evaporate to dryness. Samples were collected by first focusing on a single sample area using the selective area aperture in bright field at a magnification of 60,000 X. The instrument was then placed in diffraction mode to observe the diffraction rings at a camera length of 40 cm. Using the objective area aperture, the beam was focused on the outer diffraction rings to avoid amorphous signal near the first diffraction ring. The instrument was then placed in dark field mode to collect an image at that unique position. This process was repeated in a clockwise manner to obtain data for each position around the entire diffraction ring for a single sample.

## Inductively coupled plasma mass spectrometry

A series of films prepared on FTO substrates were cut to  $\approx$ 1 cm<sup>2</sup> in size with a uniform TiO<sub>2</sub> coating. ImageJ analysis was used to account for the specific substrate area. These films in addition to FTO samples absent of TiO<sub>2</sub> coating were heated at 180°C for 6 h in a Teflon-lined bomb with a 1:3:0.05 mL solution of 70 wt% nitric acid, 37 wt% trace metal grade HCl, 48 wt% trace metal grade HF, respectively. After heating the solutions were diluted with X purity water to a 50 mL total volume and subsequently measured using a Thermo-Finnigan Element XR ICP-MS. The instrument was calibrated using a range of concentrations spanning those of the measured samples ( $\sim$ 0–30 ug of TiO<sub>2</sub>). The resulting mass data were used to determine the average mass per area for each M:T condition. There was no significant difference in mass between calcination temperatures for each M:T.

## Electrode preparation

FTO substrates (TEC-15, Hartford Glass, CT) were rinsed and scrubbed with DI water using Kimwipes until scrubbing produces an audible squeaking noise followed by rinsing and scrubbing with IPA wetted Kimwipes again in the same manner. The substrates were then sonicated in a soapy water bath (2 g/L deconex) for 30 min. The water and alcohol scrub and rinse steps were repeated as before. The resulting substrates were stored submerged in IPA until near the time of spin coating. Just prior to coating, the FTO substrates were removed from IPA, blown dry. The FTO substrates were held at 110°C until the moment they were used for spin coating. An uncoated area for electrical contact was maintained by

masking part of the substrate with high-temperature Kapton tape as described previously.<sup>[27]</sup> After spin coating and aging as described above, the edges of the FTO substrates were cleaved to remove edge effects<sup>[58]</sup> where residual template solution can collect at the substrate edges, resulting in a locally varied film thickness. The back of each film was engraved with identifying marks for M:T, recipe number, and film number. The Kapton mask was then removed. The  $\approx$ 1 mm portion of the film proximal to the Kapton mask exhibited an edge effect with local variation of film thickness and was removed by scraping away oxide film with glass prior to calcination as described in previous work.<sup>[27]</sup> The final active area of each sample was determined by photography over a ruled grid and was analyzed using ImageJ.

## Electrochemical analysis

Electrochemical measurements were conducted using a three-electrode setup with a BioLogic SP-150 potentiostat. All measurements were performed in an argon-filled glovebox (<1 ppm O<sub>2</sub>, <1 ppm H<sub>2</sub>O). The working electrodes were porous TiO<sub>2</sub> prepared using PMT on FTO substrates. The working electrode was held by a home-built titanium metal clamp to assure ohmic contact to the FTO. All potentials are reported versus a Li/Li<sup>+</sup> reference electrode. The counter electrode was also lithium foil  $\approx$ 540 mm<sup>2</sup> in surface area. All lithium foils were scraped until shiny just prior to immersion in electrolyte. The electrolyte solution was 1.0 M LiClO<sub>4</sub> in propylene carbonate. A series of diagnostic cyclic voltammograms and electric impedance spectroscopy measurements were used to verify ohmic contact. The working electrode was then held at 1.5 V for 20 min before cycling from 1.5 to 2.5 V repeatedly 20 times at 25 mV/s to remove trace contaminants. For the MT1.6 sample temperature series, a series of 14 logarithmically spaced sweeps ranging in rate from 2.5 to 1000 mV/s in order from low to high were run, starting at 1.5 V vs. Li/Li<sup>+</sup>. There was a 3-minute voltage hold period at the end of each period, sufficient to intercalate or deintercalation  $\geq$ 99% of reversible Li species in all cases. For the M:T sample series, a series of 24 logarithmically spaced sweeps ranging in rate from 380 to 2.0 mV/s in order from high to low were run, starting at 1.5 V vs. Li/Li<sup>+</sup>. There was a 3-minute voltage hold period at the end of each period, sufficient to intercalate or deintercalation  $\geq$ 99% of reversible Li species in all cases. Mass normalization of data was based upon the film area and ICP-measurements of representative samples for each M:T sample condition. Coulombic phase content was calculated by a MATLAB baseline function using linear interpolation between the inflection point after the amorphous peak and the "tail" after the anatase peak (see Figure S4), this curve was used as a "baseline correction" to subtract amorphous CV contribution. Anatase and amorphous coulombic content were assigned as a fraction of the integrated curve assigned to anatase relative to the CV data and the difference thereof.

## Acknowledgements

W.v.d.B. and M.S. acknowledge support by the NSF CAREER program, NSF Award No. DMR-1752615. This work made use of the South Carolina SAXS Collaborative (SCSC). T.L. and M.S. acknowledge support by NSF-OIA-1655740. The authors acknowledge M.L. Myrick for access to their J.A. Woollam Co. V-VASE ellipsometer.

## Conflict of Interest

The authors declare no conflict of interest.

## Data Availability Statement

The data that support the findings of this study are available from the corresponding author upon reasonable request.

**Keywords:** amorphization • lithium-ion • nanomaterials • pseudocapacitance • titania

- [1] D. Larcher, J.-M. Tarascon, *Nat. Chem.* **2015**, *7*, 19.
- [2] J.-M. Tarascon, M. Armand, In *Materials for Sustainable Energy*, Co-Published with Macmillan Publishers Ltd, UK, **2010**, pp. 171–179.
- [3] J.-M. Tarascon, *Joule* **2020**, *4*, 1616.
- [4] H. Li, A. Liu, N. Zhang, Y. Wang, S. Yin, H. Wu, J. R. Dahn, *Chem. Mater.* **2019**, *31*, 7574.
- [5] C. Choi, D. S. Ashby, D. M. Butts, R. H. DeBlock, Q. Wei, J. Lau, B. Dunn, *Nat. Rev. Mater.* **2020**, *5*, 5.
- [6] J. B. Goodenough, *Acc. Chem. Res.* **2013**, *46*, 1053.
- [7] T. Brezesinski, J. Wang, S. H. Tolbert, B. Dunn, *Nat. Mater.* **2010**, *9*, 146.
- [8] S. Fleischmann, J. B. Mitchell, R. Wang, C. Zhan, D. Jiang, V. Presser, V. Augustyn, *Chem. Rev.* **2020**, *120*, 6738.
- [9] C. Costentin, T. R. Porter, J.-M. Savéant, *ACS Appl. Mater. Interfaces* **2017**, *9*, 8649.
- [10] G. Z. Chen, *Prog. Nat. Sci.* **2013**, *23*, 245.
- [11] E. Lim, H. Kim, C. Jo, J. Chun, K. Ku, S. Kim, H. I. Lee, I.-S. Nam, S. Yoon, K. Kang, J. Lee, *ACS Nano* **2014**, *8*, 8968.
- [12] E. Lim, W.-G. Lim, C. Jo, J. Chun, M.-H. Kim, K. Chul Roh, J. Lee, *J. Mater. Chem. A* **2017**, *5*, 20969.
- [13] K. Lan, L. Liu, J.-Y. Zhang, R. Wang, L. Zu, Z. Lv, Q. Wei, D. Zhao, *J. Am. Chem. Soc.* **2021**, jacs.1c03433.
- [14] E. Lim, C. Jo, J. Lee, *Nanoscale* **2016**, *8*, 7827.
- [15] X. Wu, J. J. Hong, W. Shin, L. Ma, T. Liu, X. Bi, Y. Yuan, Y. Qi, T. W. Surta, W. Huang, J. Neuefeind, T. Wu, P. A. Greaney, J. Lu, X. Ji, *Nat. Energy* **2019**, *4*, 123.
- [16] S. Zhang, G. Liu, W. Qiao, J. Wang, L. Ling, *J. Colloid Interface Sci.* **2020**, *562*, 193.
- [17] Z. Liu, W. Dong, J. Wang, C. Dong, Y. Lin, I.-W. Chen, F. Huang, *iScience* **2020**, *23*, 100767.
- [18] X. Zhai, J. Liu, Y. Zhao, C. Chen, X. Zhao, J. Li, H. Jin, *Appl. Surf. Sci.* **2020**, *499*, 143905.
- [19] H.-S. Kim, J. B. Cook, H. Lin, J. S. Ko, S. H. Tolbert, V. Ozolins, B. Dunn, *Nat. Mater.* **2017**, *16*, 454.
- [20] J.-Y. Shin, J. H. Joo, D. Samuelis, J. Maier, *Chem. Mater.* **2012**, *24*, 543.
- [21] T. Xia, W. Zhang, J. B. Murowchick, G. Liu, X. Chen, *Adv. Energy Mater.* **2013**, *3*, 1516.
- [22] Y. Liu, Z. Wang, J.-P. M. Veder, Z. Xu, Y. Zhong, W. Zhou, M. O. Tade, S. Wang, Z. Shao, *Adv. Energy Mater.* **2018**, *8*, 1702604.
- [23] D. Yan, A.-H. Lu, Z.-Y. Chen, L. He, W.-C. Li, *ACS Appl. Energ. Mater.* **2021**, *4*, 1824.
- [24] M. Wagemaker, W. J. H. Borghols, F. M. Mulder, *J. Am. Chem. Soc.* **2007**, *129*, 4323.
- [25] L. Zhong, Y. Liu, W.-Q. Han, J. Y. Huang, S. X. Mao, *Adv. Mater.* **2017**, *29*, 1700236.
- [26] C. Zhu, R. E. Usiskin, Y. Yu, J. Maier, *Science* **2017**, 358.
- [27] W. van den Bergh, H. N. Lokupitiya, N. A. Vest, B. Reid, S. Guldin, M. Stefić, *Adv. Funct. Mater.* **2021**, *31*, 2007826.
- [28] J. S. Ko, C.-H. Lai, J. W. Long, D. R. Rolison, B. Dunn, J. Nelson Weker, *ACS Appl. Mater. Interfaces* **2020**, *12*, 14071.
- [29] J. Ye, P. Shea, A. C. Baumgaertel, S. A. Bonev, M. M. Biener, M. Bagge-Hansen, Y. M. Wang, J. Biener, B. C. Wood, *Chem. Mater.* **2018**, *30*, 8871.
- [30] J. W. Long, B. Dunn, D. R. Rolison, H. S. White, *Adv. Energy Mater.* **2020**, *10*, 2002457.
- [31] H. Lindström, S. Södergren, A. Solbrand, H. Rensmo, J. Hjelm, A. Hagfeldt, S.-E. Lindquist, *J. Phys. Chem. B* **1997**, *101*, 7717.
- [32] S. Yoon, C. W. Lee, S. M. Oh, *J. Power Sources* **2010**, *195*, 4391.
- [33] M. Kaus, J. Kowal, D. U. Sauer, *Electrochim. Acta* **2010**, *55*, 7516.
- [34] R. L. Spyker, R. M. Nelms, *IEEE Trans. Aerosp. Electron. Syst.* **2000**, *36*, 829.
- [35] M. Z. Bazant, K. Thornton, A. Ajdari, *Phys. Rev. E* **2004**, *70*, 021506.
- [36] K. T. Chu, M. Z. Bazant, *Phys. Rev. E* **2006**, *74*, 011501.
- [37] L. Høgaard Olesen, M. Z. Bazant, H. Bruus, *Phys. Rev. E* **2010**, *82*, 011501.
- [38] J. S. Ko, M. B. Sassin, J. F. Parker, D. R. Rolison, J. W. Long, *Sustain. Energy Fuels* **2018**, *2*, 626.
- [39] B.-A. Mei, J. Lau, T. Lin, S. H. Tolbert, B. S. Dunn, L. Pilon, *J. Phys. Chem. C* **2018**, *122*, 24499.
- [40] B.-A. Mei, L. Pilon, *Electrochim. Acta* **2017**, *255*, 168.
- [41] B.-A. Mei, O. Munteşari, J. Lau, B. Dunn, L. Pilon, *J. Phys. Chem. C* **2018**, *122*, 194.
- [42] Z. Chen, H. Li, X. Lu, L. Wu, J. Jiang, S. Jiang, J. Wang, H. Dou, X. Zhang, *ChemElectroChem* **2018**, *5*, 1516.
- [43] G. Wang, Y. Ling, Y. Li, *Nanoscale* **2012**, *4*, 6682.
- [44] M. Dieterle, G. Weinberg, G. Mestl, *Phys. Chem. Chem. Phys.* **2002**, *4*, 812.
- [45] J.-Y. Shin, D. Samuelis, J. Maier, *Solid State Ionics* **2012**, *225*, 590.
- [46] D. Lee, H. Lee, Y.-T. Kim, K. Lee, J. Choi, *Electrochim. Acta* **2020**, *330*, 135192.
- [47] J. A. Yuwono, P. Burr, C. Galvin, A. Lennon, *ACS Appl. Mater. Interfaces* **2021**, *13*, 1791.
- [48] C. Arrouvel, T. C. Peixoto, M. E. G. Valerio, S. C. Parker, *Comput. Theor. Chem.* **2015**, *1072*, 43.
- [49] H. Kaper, S. Sallard, I. Djerdj, M. Antonietti, B. M. Smarsly, *Chem. Mater.* **2010**, *22*, 3502.
- [50] D. Fattakhova-Rohlfing, M. Wark, T. Brezesinski, B. M. Smarsly, J. Rathouský, *Adv. Funct. Mater.* **2007**, *17*, 123.
- [51] J. Procházka, L. Kavan, M. Zukalová, O. Frank, M. Kalbáč, A. Zukal, M. Klementová, D. Carbone, M. Graetzel, *Chem. Mater.* **2009**, *21*, 1457.
- [52] M. Zukalová, M. Kalbáč, L. Kavan, I. Exnar, M. Graetzel, *Chem. Mater.* **2005**, *17*, 1248.
- [53] L. Kavan, M. Kalbáč, M. Zukalová, I. Exnar, V. Lorenzen, R. Nesper, M. Graetzel, *Chem. Mater.* **2004**, *16*, 477.
- [54] V. Augustyn, P. Simon, B. Dunn, *Energy Environ. Sci.* **2014**, *7*, 1597.
- [55] J. Xie, P. Yang, Y. Wang, T. Qi, Y. Lei, C. M. Li, *J. Power Sources* **2018**, *401*, 213.
- [56] K. A. Lantz, N. B. Clamp, W. van den Bergh, A. Sarkar, M. Stefić, *Small* **2019**, *15*, 1900393.
- [57] H. N. Lokupitiya, A. Jones, B. Reid, S. Guldin, M. Stefić, *Chem. Mater.* **2016**, *28*, 1653.
- [58] A. Sarkar, M. Stefić, *J. Mater. Chem. A* **2017**, *5*, 11840.
- [59] A. Sarkar, A. Thyagarajan, A. Cole, M. Stefić, *Soft Matter* **2019**, *15*, 5193.
- [60] A. Sarkar, L. Evans, M. Stefić, *Langmuir* **2018**, *34*, 5738.
- [61] E. R. Williams, P. L. McMahon, J. E. Reynolds, J. L. Snider, V. Stavila, M. D. Allendorf, M. Stefić, *Mater. Adv.* **2021**, 10.1039/D1MA00146 A.
- [62] W. van den Bergh, E. R. Williams, N. A. Vest, P.-H. Chiang, M. Stefić, *Langmuir* **2021**.
- [63] M. C. Orilall, U. Wiesner, *Chem. Soc. Rev.* **2011**, *40*, 520.
- [64] M. Stefić, *J. Mater. Res.* **2021**.
- [65] E. J. W. Crossland, P. Cunha, S. Ludwigs, M. A. Hillmyer, U. Steiner, *ACS Appl. Mater. Interfaces* **2011**, *3*, 1375.
- [66] E. J. W. Crossland, M. Nedelcu, C. Ducati, S. Ludwigs, M. A. Hillmyer, U. Steiner, H. J. Snaith, *Nano Lett.* **2009**, *9*, 2813.
- [67] R. Dehmel, J. A. Dolan, Y. Gu, U. Wiesner, T. D. Wilkinson, J. J. Baumberg, U. Steiner, B. D. Wilts, I. Gunkel, *Macromolecules* **2017**, *50*, 6255.
- [68] P. Docampo, S. Guldin, M. Stefić, P. Tiwana, M. C. Orilall, S. Hüttner, H. Sai, U. Wiesner, U. Steiner, H. J. Snaith, *Adv. Funct. Mater.* **2010**, *20*, 1787.
- [69] O. Kim, S. Y. Kim, J. Lee, M. J. Park, *Chem. Mater.* **2016**, *28*, 318.
- [70] M. Nedelcu, J. Lee, E. J. W. Crossland, S. C. Warren, M. C. Orilall, S. Guldin, S. Hüttner, C. Ducati, D. Eder, U. Wiesner, U. Steiner, H. J. Snaith, *Soft Matter* **2008**, *5*, 134.
- [71] P. Sutton, P. Bennington, S. N. Patel, M. Stefić, U. B. Wiesner, P. F. Nealey, U. Steiner, I. Gunkel, *Adv. Funct. Mater.* **2019**, *29*, 1905977.
- [72] A. Vu, Y. Qian, A. Stein, *Adv. Energy Mater.* **2012**, *2*, 1056.
- [73] T. Marks, S. Trussler, A. J. Smith, D. Xiong, J. R. Dahn, *J. Electrochem. Soc.* **2011**, *158*, A51.
- [74] V. Murray, D. S. Hall, J. R. Dahn, *J. Electrochem. Soc.* **2019**, *166*, A329.

- [75] P. Mohapatra, S. Shaw, D. Mendivelso-Perez, J. M. Bobbitt, T. F. Silva, F. Naab, B. Yuan, X. Tian, E. A. Smith, L. Cademartiri, *Nat. Commun.* **2017**, *8*, 2038.
- [76] B. Reid, A. Taylor, A. Alvarez-Fernandez, M. H. Ismael, S. Sharma, B. Schmidt-Hansberg, S. Guldin, *ACS Appl. Mater. Interfaces* **2019**, *11*, 19308.
- [77] C. Robertus, W. H. Philipse, J. G. H. Joosten, Y. K. Levine, *J. Chem. Phys.* **1989**, *90*, 4482.
- [78] W. van den Bergh, S. Wechsler, H. N. Lokupitiya, L. Jarocha, K. Kim, J. Chapman, K. E. Kweon, B. C. Wood, S. Heald, M. Stefić, *Batteries Supercaps* **2022**, *a*, e202200056.
- [79] L. Kavan, J. Rathouský, M. Grätzel, V. Shklover, A. Zukal, *J. Phys. Chem. B* **2000**, *104*, 12012.
- [80] R. Marchand, L. Brohan, M. Tournoux, *Mater. Res. Bull.* **1980**, *15*, 1129.
- [81] M. Kobayashi, V. V. Petrykin, M. Kakihana, K. Tomita, M. Yoshimura, *Chem. Mater.* **2007**, *19*, 5373.
- [82] A. G. Dylla, J. A. Lee, K. J. Stevenson, *Langmuir* **2012**, *28*, 2897.
- [83] L. Kavan, *Chem. Rec.* **2012**, *12*, 131.
- [84] Y. Chimupala, P. Junploy, T. Hardcastle, A. Westwood, A. Scott, B. Johnson, R. Brydson, *J. Mater. Chem. A* **2016**, *4*, 5685.
- [85] W. V. Metanomski, Ed., *Compendium of Macromolecular Nomenclature*, 1st ed., International Union of Pure and Applied Chemistry, 1991.
- [86] S. Liang, X. Wang, Y.-J. Cheng, Y. Xia, P. Müller-Buschbaum, *Energy Storage Mater.* **2021**.
- [87] G. Gregori, R. Merkle, J. Maier, *Prog. Mater. Sci.* **2017**, *89*, 252.
- [88] A. R. Armstrong, G. Armstrong, J. Canales, R. García, P. G. Bruce, *Adv. Mater.* **2005**, *17*, 862.
- [89] X. Xin, X. Zhou, J. Wu, X. Yao, Z. Liu, *ACS Nano* **2012**, *6*, 11035.
- [90] H. Han, T. Song, E.-K. Lee, A. Devadoss, Y. Jeon, J. Ha, Y.-C. Chung, Y.-M. Choi, Y.-G. Jung, U. Paik, *ACS Nano* **2012**, *6*, 8308.
- [91] W. Li, F. Wang, S. Feng, J. Wang, Z. Sun, B. Li, Y. Li, J. Yang, A. A. Elzatahry, Y. Xia, D. Zhao, *J. Am. Chem. Soc.* **2013**, *135*, 18300.
- [92] H. Sun, L. Mei, J. Liang, Z. Zhao, C. Lee, H. Fei, M. Ding, J. Lau, M. Li, C. Wang, X. Xu, G. Hao, B. Papandrea, I. Shakir, B. Dunn, Y. Huang, X. Duan, *Science* **2017**, *356*, 599.
- [93] D. B. G. Williams, M. Lawton, *J. Org. Chem.* **2010**, *75*, 8351.
- [94] K. A. Lantz, A. Sarkar, K. C. Littrell, T. Li, K. Hong, M. Stefić, *Macromolecules* **2018**, *51*, 6967.
- [95] H. N. Lokupitiya, M. Stefić, *Nanoscale* **2017**, *9*, 1393.
- [96] Z. Qi, I. Honma, H. Zhou, *J. Phys. Chem. B* **2006**, *110*, 10590.
- [97] Y. Sheng, L. Liang, Y. Xu, D. Wu, Y. Sun, *Opt. Mater.* **2008**, *30*, 1310.
- [98] W. Shimizu, S. Nakamura, T. Sato, Y. Murakami, *Langmuir* **2012**, *28*, 12245.
- [99] D. J. Kim, S. H. Hahn, S. H. Oh, E. J. Kim, *Mater. Lett.* **2002**, *57*, 355.
- [100] E. Haimi, H. Lipsonen, J. Larismaa, M. Kapulainen, J. Krzak-Ros, S.-P. Hannula, *Thin Solid Films* **2011**, *519*, 5882.
- [101] P. Scherrer, *Math. Phys.* **1918**, *2*, 98.
- [102] A. L. Patterson, *Phys. Rev.* **1939**, *56*, 978.

Manuscript received: March 16, 2022  
Accepted manuscript online: April 4, 2022  
Version of record online: April 21, 2022